Nanoscale

PAPER

View Article Online
View Journal | View Issue

Cite this: *Nanoscale*, 2016, **8**, 492

Glucose-functionalized Au nanoprisms for optoacoustic imaging and near-infrared photothermal therapy†

Jishu Han,[a,b] Jingjing Zhang,[a] Meng Yang,[a] Daxiang Cui*[a] and Jesus M. de la Fuente*[a,c]

Received 11th September 2015,
Accepted 22nd November 2015

DOI: 10.1039/c5nr06261f

www.rsc.org/nanoscale

Targeted imaging and tumor therapy using nanomaterials has stimulated research interest recently, but the high cytotoxicity and low cellular uptake of nanomaterials limit their bioapplication. In this paper, glucose (Glc) was chosen to functionalize Au nanoprisms (NPrs) for improving the cytotoxicity and cellular uptake of Au@PEG-Glc NPrs into cancer cells. Glucose is a primary source of energy at the cellular level and at cellular membranes for cell recognition. A coating of glucose facilitates the accumulation of Au@PEG-Glc NPrs in a tumor region much more than Au@PEG NPrs. Due to the high accumulation and excellent photoabsorbing property of Au@PEG-Glc NPrs, enhanced optoacoustic imaging of a tumor *in vivo* was achieved, and visualization of the tumor further guided cancer treatment. Based on the optical–thermal conversion performance of Au@PEG-Glc NPrs, the tumor *in vivo* was effectively cured through photothermal therapy. The current work demonstrates the great potential of Au@PEG-Glc NPrs in optoacoustic imaging and photothermal cancer therapy in future.

Introduction

Cancer is one of the most serious diseases that jeopardizes human health and leads to death, amounting to 14.1 million newly diagnosed cancer cases and 8.2 million cancer-related deaths per year according to the report of the World Health Organization.[1] With the current development of scientific progress, multidisciplinary diagnoses and treatments are researched to improve the efficacy of cancer treatment.[2–5] Among various tumor imaging methods, optoacoustic imaging, as an emerging biomedical technique, possesses high spatial resolution and strong biochemical contrast through the combined impact of ultrasound imaging and optical imaging.[6–8] Utilizing ultrasound and optical signals, high resolution images in deep tissues and background-free detection can be obtained without optical diffusion and speckle artifacts.[9,10] Therefore, optoacoustic imaging has been rapidly developed for visualizing biological structures in biomedical fields, and various exogenous absorbers in the near-infrared region known as contrast agents have also been investigated for enhancing the imaging effect.[11–13] Meanwhile, among cancer treatment methods, photothermal therapy has become a strong candidate in cancer treatment and therapy since it can induce the targeted heat destruction of tumor regions.[14–16] Photothermal therapy refers to a photosensitizer that is excited with near-infrared wavelength light, which is more penetrative and less harmful to other cells and tissues. Activation of the photosensitizer leads to an excited state that then releases heat to kill the target cells.[17,18] Now the research aim is not only the improvement of diagnosis, imaging or treatment methods, but also their combination in an all-in-one system to realize highly efficient cancer treatment. To be used in combination, both the contrast agent for optoacoustic imaging and the photosensitizer for photothermal therapy need to display near-infrared absorption. Consequently, it is of great significance to choose one material that serves as a contrast agent and photosensitizer for integrated optoacoustic imaging and photothermal therapy.

[a]*Institute of Nano Biomedicine and Engineering, Key Laboratory for Thin Film and Microfabrication Technology of the Ministry of Education, Department of Instrument Science and Engineering, School of Electronic Information and Electronic Engineering, Shanghai Jiao Tong University, Shanghai 200240, P. R. China. E-mail: dxcui@sjtu.edu.cn*

[b]*Key Laboratory of Eco-chemical Engineering, Ministry of Education, Laboratory of Inorganic Synthesis and Applied Chemistry, College of Chemistry and Molecular Engineering, Qingdao University of Science and Technology, Qingdao 266042, P. R. China*

[c]*Instituto de Ciencia de Materiales de Aragon (ICMA), CSIC/Universidad de Zaragoza, Zaragoza, 50018, Spain. E-mail: jmfuente@unizar.es*

†Electronic supplementary information (ESI) available: The evolution of the UV-vis absorption of Au NPrs by centrifugation, TEM image of PEG-capped Au NPrs, the UV-vis absorption of glucose, cytotoxicity of Au@PEG-Glc NPrs, gastric cell viabilities *versus* the concentration of Au@PEG-Glc NPrs and gastric cell viabilities filled with 80 μg Au@PEG-Glc NPrs *versus* the irradiation time, optoacoustic signals of Au NPr solution and Au@PEG NPrs. See DOI: 10.1039/c5nr06261f

To date, two-dimensional nanomaterials such as carbon nanotubes, nanocomposites, Bi_2Se_3 nanoplates, MoS_2 nanosheets[19–22] and so on have been widely applied in imaging techniques and photothermal cancer therapy because of their ultra-high specific surface area, strong near-infrared optical absorbance and excellent biocompatibility. Now the challenges faced by nanomaterials are efficient absorption of higher wavelengths by changing the morphology, and also the control of toxicity. Another promising candidate, Au-based nanomaterials, possess lower cytotoxicity, higher photostability, a surface plasmon resonance property that enhances optical–thermal conversion effectiveness, and availability in various morphologies for tuning the near-infrared absorption region, which enable the aforementioned problems to be overcome and extend their applications in photothermal therapy.[23–28] In particular, because of their tunable absorption wavelengths, Au nanomaterials have become one of the most suitable and stable photoabsorbing agents for optoacoustic imaging, thus obtaining high quality images of tumor regions.[29–31]

Current efforts in controlling the size and shape of Au nanomaterials with near-infrared absorption come with the problem of the usage of highly cytotoxic surfactants such as cetyltrimethylammonium bromide (CTAB) in standard seed-mediated growth methods,[32–35] which thus affects the cytotoxicity and cellular uptake behavior. Therefore, the employment of CTAB to prepare Au nanostructures should be avoided. The strategy of preparing high quality Au nanoprisms (NPrs) free of CTAB has been developed in our previous research.[36] Moreover, another problem is cellular uptake in the biosystem. A coating of poly(ethylene glycol) (PEG) is usually chosen to improve the stability of Au nanomaterials and maintain longer circulation time in the biosystem.[37,38] However, the difference in cellular uptake of PEG coated nanomaterials between cancer cells and normal cells is not obvious, thus surface coating materials tending towards cellular uptake should be used for imaging and photothermal therapy in tumor regions. Biological molecules such as peptides, oligonucleotides and carbohydrates have become promising candidates to modify nanomaterials due to their vital functions in living systems.[39,40] Glucose, as a carbohydrate, has many advantages such as being easy to work with and inexpensive, causing no increase of nanomaterial hydrodynamic size and having no influence on conjugation with other molecules because of its small size.[41] Particularly, glucose is a primary source of energy at the cellular level and at cellular membranes for cell recognition.[42] A coating of glucose can improve cellular uptake of nanomaterials into cancer cells.[42,43] So on the basis of our success in synthesizing various Au nanomaterials in aqueous solution,[36] in this work, we demonstrate a facile and feasible method to synthesize Au NPrs in aqueous solution on the basis of a one-pot reduction of Au ions using sodium thiosulfate. The efficient absorption of near-infrared wavelengths is achieved due to the high anisotropic shape of the NPrs. Without the usage of the surfactant CTAB, the cytotoxicity of the Au NPrs obviously lowers, and the glucose coating effectively improves cancer cellular uptake, thus giving the as-prepared Au NPrs an excellent performance for applications in optoacoustic imaging and photothermal cancer therapy.

Experimental section

Materials

Hydrogen tetrachloroaurate(III) hydrate ($HAuCl_4{\cdot}4H_2O$), sodium thiosulfate ($Na_2S_2O_3$), $NaBH_4$ (96%), KI (98%), NaOH (99%) and all the other chemicals used were purchased from the Sinopharm Chemical Reagent Co., Ltd. *N*-Hydroxysulfosuccinimide (NHS), 1-ethyl-3-[3-dimethylaminopropyl] carbodiimide hydrochloride (EDC), glucose (4-aminophenyl β-D-glucopyranoside, Glc), and 2-(*N*-morpholino)ethanesulfonic acid (MES) were purchased from Sigma-Aldrich and used as received. HS–C_2H_4–CONH–PEG–O–C_3H_6–COOH (HS–PEG–COOH, MW = 5000 g mol^{-1}) was obtained from Rapp-Polymere.

Synthesis of Au nanoprisms

The synthesis of aqueous Au NPrs followed a modified preparation by Pelaz *et al.*[36] In brief, aqueous Au NPrs were prepared by dropwise adding 12 mL of freshly prepared 0.5 mM $Na_2S_2O_3$ solution and 32.7 μL of 0.01 M KI to 10 mL of 2 mM $HAuCl_4$ solution. The solution was mildly stirred for 9 min. Then, 2 mL of 0.5 mM $Na_2S_2O_3$ solution was added and the final solution was stirred for 90 min.

Synthesis of PEGylated Au NPrs

Au NPrs were stabilized with HS–PEG–COOH modification. Briefly, 1 mg of PEG was added into 10 mL of the prepared Au NPr solution. The pH was adjusted to 12.0 with 2 M NaOH. Subsequently, the solution was sonicated for 1 hour at 60 °C. The PEGylated Au NPrs were purified by centrifugation at 6000 rpm for 10 min three times.

Synthesis of Au@PEG-Glc NPrs

The PEGylated Au NPrs were functionalized with glucose to promote cellular uptake. Typically, 1 mg of the PEGylated Au NPrs was dispersed in 2 mL of MES buffer (pH = 6.0) and incubated with 0.5 mg of EDC and 1 mg of NHS for 20 min. The activated Au NPrs were centrifuged at 6000 rpm for 10 min to remove the excess EDC and NHS, and then incubated with 0.5 mg of 4-aminophenyl β-D-glucopyranoside for 2 hours. The Glc-functionalized NPrs were washed three times by centrifugation.

Characterization

UV-visible absorption spectra were obtained using a Varian Cary 50 spectrophotometer (Varian Inc., Palo Alto, CA, USA). Field emission scanning electron microscopy (FESEM) was conducted using a Zeiss Ultra electron microscope operated at 30 kV. FTIR spectra were taken using a Nicolet 6700 spectrometer (Thermo Electron Corporation, Madison, WI, USA) using KBr pellets. Cells were observed using a fluorescence

microscope (NIKON TS100-F), and imaged using a GE HDX 3.0 T MR imaging instrument equipped with ParaVision 3.0 software. Photoacoustic (PA) imaging of the probes was accomplished using an Endra Nexus 128 PA scanner.

Cell culture and MTT assay

The human gastric cancer cell line MGC-803 cells were incubated at 37 °C (5% CO_2) in Dulbecco's Modified Eagle's Medium (DMEM, HyClone) supplemented with 10% (vol/vol) fetal bovine serum (Gibco) and 100 U mL^{-1} penicillin–streptomycin. The MTT assay was carried out to investigate the toxicity of the as-prepared NPrs. In brief, MGC-803 cells were seeded in a 96-well plate at a density of 5000 cells per well and cultured overnight. The cells were incubated with serial concentrations of Au@PEG or Au@PEG-Glc NPrs for 24 hours. Then, the cells were washed with PBS and the medium was removed. Cytotoxicity was evaluated by a standard MTT assay. Cell viability = (OD570 nm of the experimental group/OD570 nm of the control group) × 100%, and the cell viability of the control group was denoted as 100%.

In vitro photothermal ablation of MGC-803 cells

The MGC-803 cells were seeded into 96-well plates and incubated for 24 h to allow the cells to be attached. Then, the medium was carefully removed and fresh medium containing different concentrations of Au@PEG or Au@PEG-Glc NPrs was added into each well. After incubation for another 24 h, the cells were washed to remove non-internalized NPrs and irradiated for different times by an 808 nm laser with an output power density of 0.5 W cm^{-2}. Then, the cells were incubated for an extra 12 hours and cell viability was measured *via* the MTT assay according to the procedure described above.

Simultaneously, green fluorescent protein (GFP)-transfected MGC-803 cells were incubated and treated in the same way as MGC-803 cells, then Propidium Iodide (PI) was used to stain dead cells before observation by fluorescence microscopy.

In vivo optoacoustic imaging

Animal experiments were performed according to Guidelines for Animal Care and Use Committee, Shanghai Jiao Tong University. Male athymic nude mice were obtained from Shanghai LAC Laboratory Animal Co. Ltd, Chinese Academy of Sciences (Shanghai, China). MGC-803 cells (1×10^6) were injected subcutaneously into the right posterior flank area of male nude mice aged 4 to 5 weeks. Tumors were allowed to grow to a diameter of approximately 5 mm. MGC-803 cell tumor-bearing nude mice were first anaesthetized by intraperitoneal injection of pentobarbital sodium (40 mg kg^{-1}), then a PBS solution of Au@PEG or Au@PEG-Glc NPrs (100 μL, 1 mg mL^{-1}) was intravenously injected into the mice. Then, the imaging target (tumor) was well mounted in the protruding top of the bowl. The image position was consistent to facilitate comparisons. The protruding top of the bowl was immersed in water and the interface between the slot and imaging target was free of bubbles, providing excellent photoacoustic signal transduction. Finally, optoacoustic imaging of the image target was acquired according to different injection times. Pre-injection scans were used as controls.

In vivo photothermal imaging

MGC-803 cell tumor-bearing nude mice were first anaesthetized by intraperitoneal injection of pentobarbital sodium (40 mg kg^{-1}), then a PBS solution of Au@PEG or Au@PEG-Glc NPrs (100 μL, 1 mg mL^{-1}) was intravenously injected into the mice. Mice intravenously injected with PBS (100 μL) were used as a control. After 24 hours, the tumor site was exposed to an 808 nm laser with an output power density of 0.5 W cm^{-2} for 5 min. During the process of laser radiation, temperature and whole-body infrared images were captured by a thermal imaging camera (Testo 875-1, Germany) at different time points.

The tumor size of all the mice was measured and pictures of the mice were taken at pre-determined time points. The length and width of the tumors were measured using a digital vernier caliper and the tumor volumes were calculated according to the formula (tumor length × (tumor width)^2)/2.

Results and discussion

As mentioned in the Experimental section, the Au NPrs are synthesized in $HAuCl_4$ solution through stepwise addition of sodium thiosulfate. For a typical synthesis of Au NPrs, 20 mL of aqueous solution containing 2 mM $HAuCl_4$ is mixed with 0.5 mM $Na_2S_2O_3$ solution and 0.1 M KI under vigorous stirring. The addition makes the mixture gradually turn from pale brown to brownish black. After 9 min, additional 0.5 mM $Na_2S_2O_3$ solution was added dropwise and the mixture was kept stirring for 60 min to maintain the growth of Au NPrs. Fig. 1a shows the UV-vis absorption spectrum of the Au NPrs with a major plasmon band at 845 nm, corresponding to the in-plane dipolar band of the Au NPrs. The band at 530 nm is attributed to the byproducts of the Au nanoparticles.[44] From the SEM image and AFM measurement, it is found that the as-prepared Au NPrs are flat NPs with three congruent edge lengths of 94 nm and thicknesses of 10 nm (Fig. 1b, c and e). Compared with nanorods, nanocubes, or nanospheres, the triangular shaped structure with high truncations and aspect ratio and three tips displays stronger electromagnetic field enhancement and provides more distinct plasmon resonance in the near-infrared region.[45–49] High-resolution TEM shows that the triangular faces are [111] with a lattice spacing of 1.44 Å, consisting of the (220) plane of fcc Au (Fig. 1d),[50] and electron diffraction analysis of an individual gold nanoprism shows that it is single crystalline and that the flat top and bottom faces are [111] facets (Fig. 1f).[51] Due to no surfactant being added in our experiment, the colloidal syntheses of triangular nanoprisms tend to yield some percentage of nanohexagons or nanodisks.[52,53] Based on this, it is necessary to purify the NPrs through centrifugation. Fig. S1† shows that centrifugation can remove smaller nanostructures and make the NPrs more homogeneous.

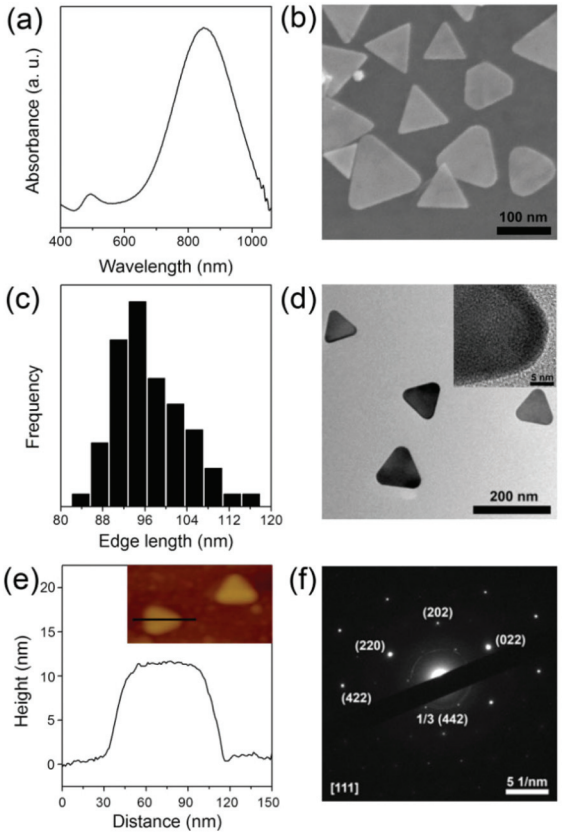

Fig. 1 UV-vis absorption spectrum (a), SEM image (b), size distribution (c) and TEM image (inset: HRTEM image of the top-facet of a NPr) of Au NPrs (d); height profile along the solid line in the AFM image (inset) of a single Au NPr (e) and electron diffraction pattern of the top of a single prism (f).

To further increase the colloidal stability of Au NPrs, the NPrs were modified with bifunctional polyethylene glycol. As shown in the TEM image, the Au NPrs are covered with a shell with low contrast, since the contrast of polymer materials is usually worse than that of inorganic materials (Fig. S2†). The coating of the PEG layer enhances the colloidal stability of the Au NPrs obviously, thus avoiding morphology variation toward spherical particles and final aggregation.[54] UV-vis spectra also exhibit unchanged absorption properties (Fig. S3†). To increase the biocompatibility and cellular uptake for further biological application, glucose is chosen to bond to the surface of the Au@PEG NPrs. Glucose is one of the most important molecules in the biosystem as it is a primary source of energy at the cellular level. Cancer cell growth is heavily dependent on increased glucose metabolism.[42,43] Moreover, overexpression of membrane glucose transporters such as GLUT-1 in human cancers causes increased glucose utilization in tumor cells.[55] So, a coating of glucose can increase biocompatibility and cellular uptake, and reduce cytotoxicity effectively for further biological application.[56] UV-vis absorption and FTIR spectra of the Au@PEG NPrs and Au@PEG-Glc NPrs are compared to prove the formation of an amido bond (Fig. 2). The absorption peak at 280 nm indicates the existence

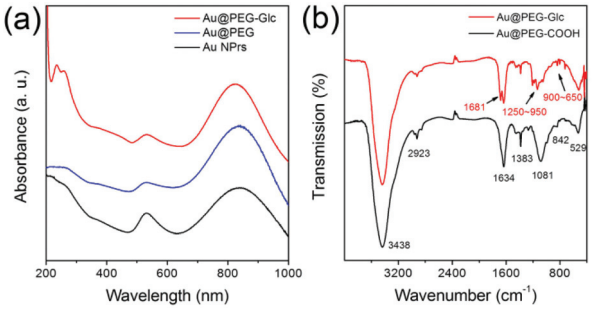

Fig. 2 (a) The evolution of the UV-vis absorption of Au NPrs without modification (black), modified with PEG (blue), and modified with glucose (red). (b) FTIR spectra of the Au@PEG-COOH and Au@PEG-Glc NPrs.

of glucose (Fig. S4†), and is the characteristic absorption peak of the phenyl group from 4-aminophenyl β-D-glucopyranoside, and the changes in the FTIR spectra illustrate the formation of an amido bond between PEG and glucose. Enhanced structural stability and biocompatibility will broaden the practical applications of Au@PEG-Glc NPrs in optoacoustic imaging and photothermal therapy.

As mentioned above, Au nanomaterials can absorb NIR light and transform the energy into heat.[23–28] Au NPrs with high truncations and aspect ratio and three tips possess enhanced plasmon resonance in the near-infrared region.[45–49] They are expected to be an efficient nanoheater to kill cancer cells. The photothermal conversion performance is monitored by the temperature change of 0.5 mL of Au@PEG-Glc NPr solution (Fig. 3). NPr solutions of concentrations varying from 5 μg mL^{-1} to 160 μg mL^{-1} were irradiated under an 808 nm laser with a density of 0.5 W cm^{-2}. The temperature increased obviously during the first 5 minutes and kept steady subsequently. The temperature increment rises from 12.4 to 20.2 °C after laser irradiation. Actually, the temperature

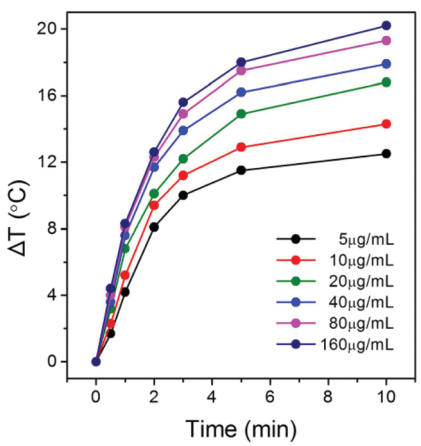

Fig. 3 Temperature increment of the Au@PEG-Glc NPrs at different concentrations under an 808 nm laser.

increment of the Au@PEG-Glc NPrs can be raised more under laser irradiation with a higher density. Hyperthermia is known to induce cell death at temperatures between 42 and 47 °C.[57,58] Excessively high temperature would lead to healthy cells being damaged. Herein, the laser density and NPr concentrations are chosen for the required temperature rise for more efficient cancer photothermal therapy.

The photothermal conversion performance of Au@PEG-Glc NPrs indicates their feasibility as a nanoheater. The biocompatibility of nanostructures is also an important issue for further *in vivo* applications in imaging and therapy. The cytotoxicity of the Au@PEG-Glc NPrs was studied by means of a MTT assay (Fig. S5†). Cell viability decreased less with an increase in Au@PEG-Glc NPr concentration, and no obvious cytotoxicity was observed. Moreover, photothermal performance was evaluated by investigating the cell viability *versus* concentration of the Au@PEG-Glc NPrs and the irradiation time (Fig. S6†). With increasing the concentration of Au@PEG-Glc NPrs or extending the irradiation duration, the cell viability decreased rapidly. Namely, it depended on both NPr concentration and irradiation duration.

Fig. 4 exhibits the fluorescence live/dead cell staining experiments performed to observe the photothermal ablation process. Here, gastric cancer cells are used because gastric cancer is the third leading cause of cancer-related mortality worldwide but the efficacy of traditional therapies is not ideal.[1,59] Therefore it is important to improve the treatment efficacy of gastric cancer through novel biomedical techniques. Gastric cancer MGC-803 cells were transfected with GFP and incubated with Au@PEG NPrs and Au@PEG-Glc NPrs under laser irradiation for 2 min, 4 min and 8 min. Then the cells were stained with PI to show the changes in the cells. With extending the irradiation time, the amount of live cells labelled by green fluorescence decreases, and dead cells labelled by red fluorescence increases. In comparison, in the presence of the Au@PEG-Glc NPrs, the mortality of cancer cells reaches 80% after 4 min of irradiation, and almost 100% after 8 min of irradiation, indicating that the cancer cells are effectively killed. Moreover, cells non-treated with NPrs were unaffected under the same conditions. This result is consistent with the cell viability measured by the MTT assay (Fig. S6†), illustrating that the Au@PEG-Glc NPrs could promote cancer cell ablation under laser irradiation efficiently. In the presence of the Au@PEG NPrs, the mortality of cancer cells is only about 65% after 8 min of irradiation. This indicates that the number of Au@PEG-Glc NPrs within the cells is more than that of Au@PEG NPrs; namely the coating of glucose facilitates NPrs entering the cells.

The coating of glucose was reported to promote the cellular uptake of nanomaterials much more than that of unmodified ones by cancer cells.[42] As a carbohydrate, glucose is a fundamental source of energy in living cells. Cancer cells undergo more active metabolism than normal cells, thus taking up more glucose.[60–62] Overexpression of membrane glucose transporters in human cancers also leads to increased glucose utilization in tumor cells.[55] ICP-MS measurements indicate that cancer cells (1×10^6) take up 2.4 times more Au@PEG-Glc NPrs than Au@PEG NPrs. The modification of glucose efficiently accelerates the accumulation of Au NPrs in tumor cells. For the Au@PEG NPrs, their accumulation in tumor tissue is based only on the enhanced permeability and retention (EPR) effect in solid tumors.[63–65] So Au@PEG-Glc NPrs could be effectively delivered to cancer tissue and spread inside it much more than Au@PEG NPrs due to the combined influence of glucose and the EPR effect.

As mentioned above, Au NPrs possess not only photothermal conversion performance, but also photoabsorbing performance as an imaging agent. As shown in Fig. S7,† Au NPrs exhibit optoacoustic signals that significantly increase with an increase of Au NPr concentration. Therefore, Au NPrs can be visualized *in vivo* to evaluate the circulation time and accumulation behavior of the Au NPrs inside the tumor instead of dissecting mice and monitoring them through ICP-MS measurements, enabling the subsequent therapy to be guided. Fig. 5 shows the optoacoustic images of the tumors at

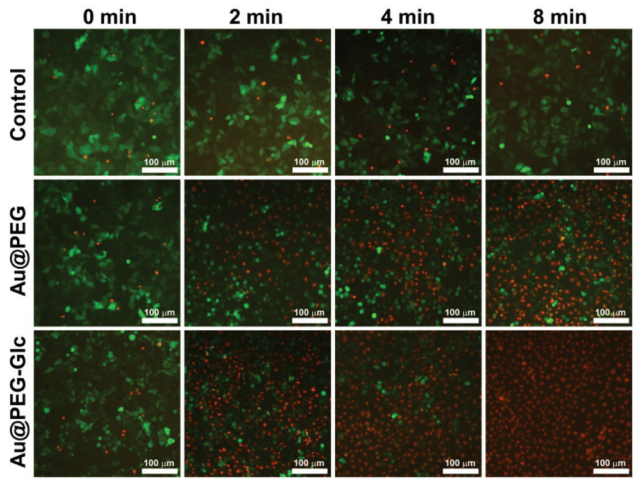

Fig. 4 Fluorescence images of cells filled with Au@PEG and Au@PEG-Glc NPrs under laser irradiation (0 min, 2 min, 4 min, 8 min), and fluorescence images of cells under laser irradiation (control group, 0 min, 2 min, 4 min, 8 min).

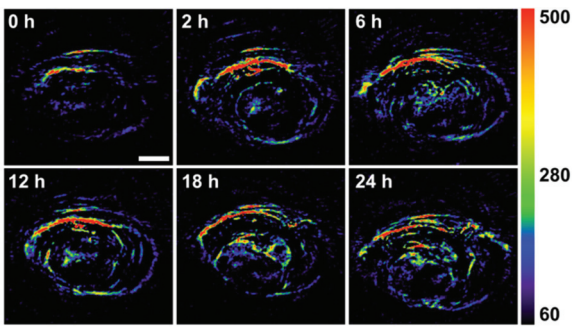

Fig. 5 Optoacoustic signals of the Au@PEG-Glc NPrs in the tumor region acquired before injection (0 h) and after injection (2, 6, 12, 18 and 24 h). The scale bar is 2 mm.

different times. Before injection, only the major blood vessels can be observed. Then, 100 μL (1 mg mL^{-1}) of the Au@PEG-Glc NPrs were intravenously injected into the MGC-803 cell tumor-bearing nude mice. The optoacoustic signals in the tumor region are enhanced much more and the profile of the tumor becomes clearer with the passage of time. In comparison, optoacoustic signals of the tumor after injection of the Au@PEG NPrs are weaker and the profile is less obvious (Fig. S8†). This demonstrates that the Au@PEG-Glc NPrs gradually accumulate in the tumor region much more and that the accumulation process can be observed by optoacoustic imaging *in vivo*.

Based on the optoacoustic imaging technique, photothermal therapy was further assessed *in vivo*. Nude mice bearing a MGC-803 tumor model were injected intravenously with 100 μL of PBS, 100 μL of a 1 mg mL^{-1} PBS solution of Au@PEG NPrs and 100 μL of a 1 mg mL^{-1} PBS solution of Au@PEG-Glc NPrs. After 24 h the tumors were exposed to an 808 nm laser at a power density of 0.5 W cm^{-2} for 5 min. As shown in Fig. 6a, the surface temperature of the tumors was monitored by a thermal imaging camera. With the injection of the Au@PEG-Glc NPrs, the temperature rapidly reached above 44 °C in 1 min, and rose to 50 °C in the next 4 min. In comparison, the temperature of the tumor injected with the Au@PEG NPrs increased to around 44 °C after 5 min irradiation (Fig. 6b). This indicates that the coating of glucose facilitates the accumulation of the Au@PEG-Glc NPrs in the tumor region and the increase of temperature after the same irradiation time, thus achieving efficient photothermal therapy. The obtained highest temperature is controlled purposely, because heating cells to between 42 and 47 °C leads to cell death,[66] and it is not necessary to generate excessively high temperatures leading to healthy tissue being seriously damaged and curable duration extended.

Through the photothermal treatment above, the therapeutic efficacy of Au@PEG-Glc NPrs is investigated by measuring the volumes of tumors. After the same duration of laser irradiation, the tumors on the mice injected with the Au@PEG-Glc NPrs are completely inhibited and the tumors disappear and are cured after 12 days (Fig. 7a). No regrowth of the tumors occurred in two months (Fig. S9†). In comparison, the tumors on the mice injected with PBS exhibit a rapid growth. The laser irradiation alone does not have an impact on the tumor growth. Meanwhile, the tumors on the mice injected with the Au@PEG NPrs are partly inhibited at first but could not be eliminated completely (Fig. 7a). This implies that the photothermal therapy effect of the Au@PEG-Glc NPrs is much better than that of the Au@PEG NPrs under the same laser irradiation; namely glucose is beneficial to increase the

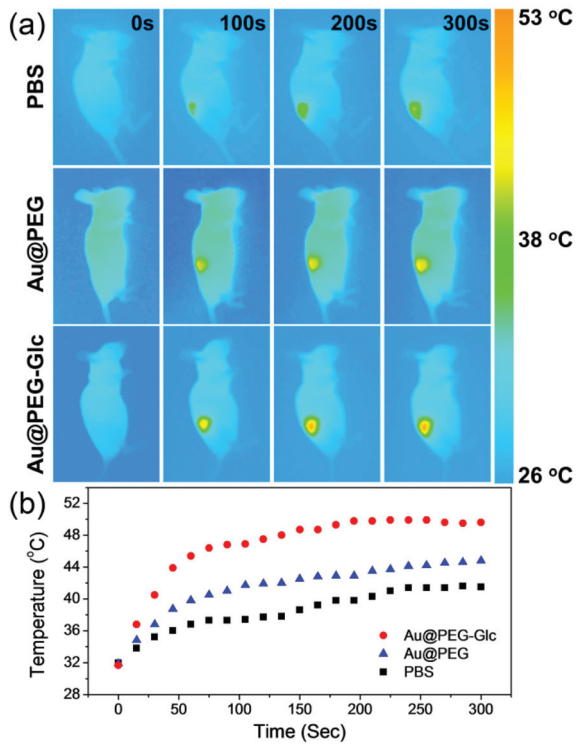

Fig. 6 (a) Representative thermal images of tumor-bearing mice exposed to an 808 nm laser (0.5 W cm^{-2}, 5 min) after injection with 100 μL of PBS (control group), Au@PEG NPrs (1 mg mL^{-1}) and Au@PEG-Glc NPrs (1 mg mL^{-1}). (b) The corresponding temperature rise profiles at the tumor site over 5 min of laser irradiation with NPrs or PBS only.

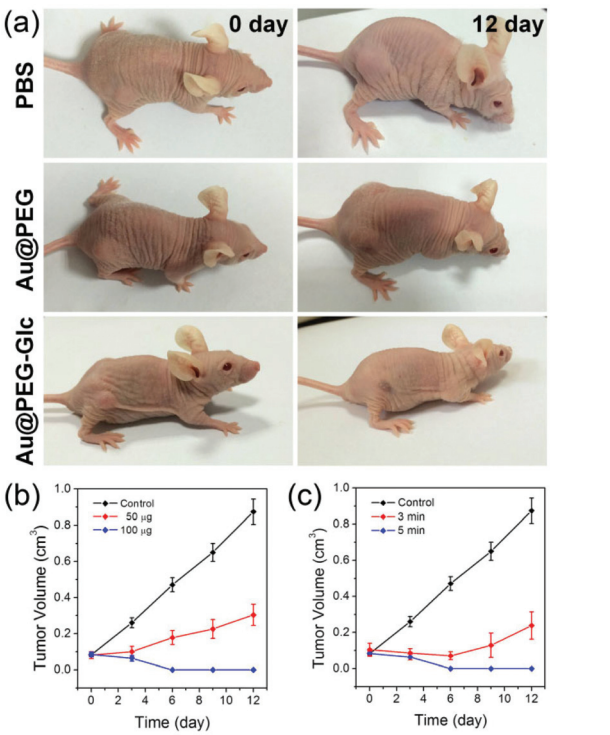

Fig. 7 Photographs of the tumor mice under different treatments at different time periods (a). The evolution of the relative tumor volume of tumor-bearing mice with the injection of different concentrations of Au@PEG-Glc NPrs (b), and the evolution of the relative tumor volume of tumor-bearing mice with different irradiation times (c).

accumulation of the Au@PEG-Glc NPrs in the tumor region and then enhance the photothermal therapy effect. Furthermore, the tumors on mice with different Au@PEG-Glc NPr concentrations or irradiation durations were studied and the tumor sizes were measured by a vernier caliper every two days (Fig. 7b and c). In contrast, the tumors with an injection of 50 μg mL^{-1} Au@PEG-Glc NPrs or 3 min irradiation show slightly slower growth compared to the control group, indicating that selection of the amount of Au@PEG-Glc NPrs and irradiation duration affects tumor therapy directly. The Au@PEG-Glc NPrs possess excellent performance in *in vivo* photothermal therapy.

Conclusions

In conclusion, we demonstrate a facile and feasible method for optoacoustic imaging and photothermal therapy of gastric cancer by employing Au@PEG-Glc NPrs prepared in aqueous solution as an imaging contrast agent and hyperthermia agent. Through a one-pot method, the Au NPrs were synthesized by a stepwise reduction of sodium thiosulfate to obtain a morphology with a near-infrared absorption property. In this synthesis method, the non-use of highly toxic surfactants decreases the cytotoxicity efficiently. Glucose is used to modify the NPr surface, thus they exhibit an excellent biocompatibility and cellular uptake. In particular, high accumulation of the Au@PEG-Glc NPrs in the tumor region is achieved, thus leading to effective optoacoustic imaging and photothermal therapy for cancer treatment. Here, a relatively lower temperature increment of the Au@PEG-Glc NPrs in photothermal therapy not only avoids damage of healthy tissue, but also possesses an obvious treatment effect for the tumor. Based on this, it is possible to apply the as-synthesized nanomaterials in biomedical imaging, drug delivery, and photothermal therapy.

Acknowledgements

This work was supported by the China National Key Basic Research Program (973 Project) (no. 2010CB933902 and 2015CB931802), National Natural Scientific Fund (no. 81225010, 81327002 and 31170961), National 863 Hi-tech Project (no. 2012AA022703 and 2014AA020700), National Natural Scientific Fund (no. 20771075 and no. 20803040), Shanghai Science and Technology Fund (no. 13NM1401500), Project funded by China Postdoctoral Science Foundation, Shanghai 1000 People Plan Program. JMF thanks the grant ERC-Starting Grant 239931-NANOPUZZLE and Fondo Social Europeo (FSE; Gobierno de Aragón).

Notes and references

1 Cancer IAfRo. Globocan 2012: Estimated cancer incidence, mortality and prevalence worldwide in 2012. World Health Organization http://globocan.iarc.fr/Pages/fact_sheets_cancer.aspx, accessed on. 2015, 6.
2 G. M. Whitesides, *Nat. Biotechnol.*, 2003, **21**, 1161–1165.
3 N. L. Rosi and C. A. Mirkin, *Chem. Rev.*, 2005, **105**, 1547–1562.
4 U. Dreshler, B. Erdogan and V. M. Rotello, *Chem. – Eur. J.*, 2004, **10**, 5570–5579.
5 C. Loo, A. Lowery, N. Halas, J. West and R. Drezek, *Nano Lett.*, 2005, **5**, 709–711.
6 L. M. Nie and X. Y. Chen, *Chem. Soc. Rev.*, 2014, **43**, 7132–7170.
7 T. Harrison, J. C. Ranasinghesagara, H. Lu, K. Mathewson, A. Walsh and R. J. Zemp, *Opt. Express*, 2009, **17**, 22041–22046.
8 L. V. Wang and S. Hu, *Science*, 2012, **335**, 1458–1462.
9 W. Li and X. Chen, *Nanomedicine*, 2015, **10**, 299–320.
10 L. H. V. Wang, *Nat. Photonics*, 2009, **3**, 503–509.
11 R. Schulze, G. Zangerl, M. Holotta, D. Meyer, F. Handle, R. Nuster, G. Paltauf and O. Scherzer, *J. Biomed. Opt.*, 2011, **16**, 086002.
12 J. A. Viator, J. Komadina, L. O. Svaasand, G. Aguilar, B. Choi and J. S. Nelson, *J. Invest. Dermatol.*, 2004, **122**, 1432–1439.
13 K. Ding, J. F. Zeng, L. H. Jing, R. R. Qiao, C. Y. Liu, M. X. Jiao, Z. Li and M. Y. Gao, *Nanoscale*, 2015, **7**, 11075–11081.
14 D. Jaque, L. Martínez Maestro, B. del Rosal, P. Haro-Gonzalez, A. Benayas, J. L. Plaza, E. Martín Rodrígueza and J. García Soléa, *Nanoscale*, 2014, **6**, 9494–9530.
15 F. Jabeen, M. Najam-ul-Haq, R. Javeed, C. W. Huck and G. K. Bonn, *Molecules*, 2014, **19**, 20580–20593.
16 S. Lal, S. E. Clare and N. J. Halas, *Acc. Chem. Res.*, 2008, **41**, 1842–1851.
17 D. Lapotko, E. Lukianova, M. Potapnev, O. Aleinikova and A. Oraevsky, *Cancer Lett.*, 2006, **239**, 36–45.
18 S. Toroghi and P. G. Kik, *Phys. Rev. B: Condens. Matter*, 2014, **90**, 205414.
19 K. Yang, S. Zhang, G. Zhang, X. Sun, S.-T. Lee and Z. Liu, *Nano Lett.*, 2010, **10**, 3318–3323.
20 J. Li, F. Jiang, B. Yang, X. R. Song, Y. Liu, H. H. Yang, D. R. Cao, W. R. Shi and G. N. Chen, *Sci. Rep.*, 2013, **3**, 1998.
21 S. S. Chou, B. Kaehr, J. Kim, B. M. Foley, M. De, P. E. Hopkins, J. Huang, C. J. Brinker and V. P. Dravid, *Angew. Chem., Int. Ed.*, 2013, **125**, 4254–4258.
22 T. Liu, C. Wang, X. Gu, H. Gong, L. Cheng, X. Z. Shi, L. Z. Feng, B. Q. Sun and Z. Liu, *Adv. Mater.*, 2014, **26**, 3433–3440.
23 Y. N. Xia, W. Li, C. M. Cobley, J. Y. Chen, X. H. Xia, Q. Zhang, M. X. Yang, E. C. Cho and P. K. Brown, *Acc. Chem. Res.*, 2011, **44**, 914–924.
24 E. Boisselier and D. Astruc, *Chem. Soc. Rev.*, 2009, **38**, 1759–1782.
25 X. M. Zhu, C. H. Fang, H. L. Jia, Y. Huang, C. H. K. Cheng, C.-H. Ko, Z. Y. Chen, J. F. Wang and Y.-X. J. Wang, *Nanoscale*, 2014, **6**, 11462–11472.
26 Z. Z. Wang, Z. W. Chen, Z. Liu, P. Shi, K. Dong, E. G. Ju, J. S. Ren and X. G. Qu, *Biomaterials*, 2014, **35**, 9678–9688.

27 I. H. El-Sayed, X. H. Huang and M. A. El-Sayed, *Cancer Lett.*, 2006, **239**, 129–135.
28 X. H. Huang, P. K. Jain, I. H. El-Sayed and M. A. El-Sayed, *Laser Med. Sci.*, 2008, **23**, 217–228.
29 M. Chen, S. H. Tang, Z. D. Guo, X. Y. Wang, S. G. Mo, X. Q. Huang, G. Liu and N. F. Zheng, *Adv. Mater.*, 2014, **26**, 8210–8216.
30 C. C. Bao, N. Beziere, P. del Pino, B. Pelaz, G. Estrada, F. R. Tian, V. Ntziachristos, J. M. de la Fuente and D. X. Cui, *Small*, 2013, **9**, 68–74.
31 A. Agarwal, S. W. Huang, M. O'Donnell, K. C. Day, M. Day, N. Kotov and S. Ashkenazi, *J. Appl. Phys.*, 2007, **102**, 064701.
32 H. J. Chen, L. Shao, Q. Li and J. F. Wang, *Chem. Soc. Rev.*, 2013, **42**, 2679–2724.
33 Y. Qiu, Y. Liu, L. M. Wang, L. G. Xu, R. Bai, Y. L. Ji, X. C. Wu, Y. L. Zhao, Y. F. Li and C. Y. Chen, *Biomaterials*, 2010, **31**, 7606–7619.
34 A. M. Alkilany, P. K. Nagaria, C. R. Hexel, T. J. Shaw, C. J. Murphy and M. D. Wyatt, *Small*, 2009, **5**, 701–708.
35 W. H. Ni, X. S. Kou, Z. Yang and J. F. Wang, *ACS Nano*, 2008, **2**, 677–686.
36 B. Pelaz, V. Grazu, A. Ibarra, C. Magen, P. del Pino and J. M. de la Fuente, *Langmuir*, 2012, **28**, 8965–8970.
37 N. A. Alcantar, E. S. Aydil and J. A. Israelachvili, *J. Biomed. Mater. Res.*, 2000, **51**, 343–351.
38 R. T. H. Chan, H. Marçal, R. A. Russell, P. J. Holden and L. J. R. Foster, *Int. J. Polym. Sci.*, 2011, **2011**, 473045.
39 R. Elghanian, J. J. Storhoff, R. C. Mucic, R. L. Letsinger and C. A. Mirkin, *Science*, 1997, **277**, 1078–1081.
40 D. A. Giljohann, D. S. Seferos, P. C. Patel, J. E. Millstone, N. L. Rosi and C. A. Mirkin, *Nano Lett.*, 2007, **7**, 3818–3821.
41 M. Moros, B. Hernáez, E. Garet, J. T. Dias, B. Sáez, V. Grazú, A. González-Fernández, C. Alonso and J. M. de la Fuente, *ACS Nano*, 2012, **6**, 1565–1577.
42 I. Sur, D. Cam, M. Kahraman, A. Baysal and M. Culha, *Nanotechnology*, 2010, **21**, 175104.
43 J. Yang, J. Zeng, T. Kong, X. Wang, W. Roa, T. El-Bialy, J. Xing and J. Chen, *LISSA 2007: IEEE Life Science Systems and Applications Workshop*, IEEE, Piscataway, NJ, 2007, 92.
44 G. K. Joshi, P. J. McClory, S. Dolai and R. Sardar, *J. Mater. Chem.*, 2012, **22**, 923–931.
45 L. J. Sherry, R. Jin, C. A. Mirkin, G. C. Schatz and R. P. Van Duyne, *Nano Lett.*, 2006, **6**, 2060–2065.
46 E. Hao and G. C. Schatz, *J. Chem. Phys.*, 2004, **120**, 357–366.
47 K. H. Lee, Q. L. Chen, C. H. Yip, Q. Yan and C. C. Wong, *Microelectron. Eng.*, 2010, **87**, 1941–1944.
48 H. Chen, X. Kou, Z. Yang, W. Ni and J. Wang, *Langmuir*, 2008, **24**, 5233–5237.
49 X. B. Xu, Z. Yi, X. B. Li, Y. Y. Wang, J. P. Liu, J. S. Luo, B. C. Luo, Y. G. Yi and Y. J. Tang, *J. Phys. Chem. C*, 2013, **117**, 17748–17756.
50 C. Xue, J. E. Millstone, S. Y. Li and C. A. Mirkin, *Angew. Chem., Int. Ed.*, 2007, **46**, 8436–8439.
51 J. E. Millstone, S. J. Hurst, G. S. Métraux, J. I. Cutler and C. A. Mirkin, *Small*, 2009, **5**, 646–664.
52 P. J. Straney, C. M. Andolina and J. E. Millstone, *Langmuir*, 2013, **29**, 4396–4403.
53 J. E. Millstone, G. S. Métraux and C. A. Mirkin, *Adv. Funct. Mater.*, 2006, **16**, 1209–1214.
54 X. G. Ding, C. H. Liow, M. X. Zhang, R. J. Huang, C. Y. Li, H. Shen, M. Y. Liu, Y. Zou, N. Gao, Z. J. Zhang, Y. G. Li, Q. B. Wang, S. Z. Li and J. Jiang, *J. Am. Chem. Soc.*, 2014, **136**, 15684–15693.
55 L. Aloj, C. Caracó, E. Jagoda, W. C. Eckelman and R. D. Neumann, *Cancer Res.*, 1999, **59**, 4709–4714.
56 A. G. Barrientos, J. M. de la Fuente, T. C. Rojas, A. Fernandez and S. Penades, *Chem. – Eur. J.*, 2001, **9**, 1909–1921.
57 C. Vauthier, N. Tsapis and P. Couvreur, *Nanomedicine*, 2011, **6**, 99–109.
58 P. Cherukuri, E. S. Glazer and S. A. Curley, *Adv. Drug Delivery Rev.*, 2010, **62**, 339–345.
59 S. Vinogradov and X. Wei, *Nanomedicine*, 2012, **7**, 597–615.
60 T. Kong, J. Zeng, X. P. Wang, X. Y. Yang, J. Yang, S. McQuarrie, A. McEwan, W. Roa, J. Chen and J. Z. Xing, *Small*, 2008, **4**, 1537–1543.
61 L. G. Baggetto, *Biochimie*, 1992, **74**, 959–974.
62 O. Warburg, K. Posener and E. Negelein, *Biochem. Z.*, 1924, **152**, 319–344.
63 Y. Matsumura and H. Maeda, *Cancer Res.*, 1986, **46**, 6387–6392.
64 R. Duncan and Y. N. Sat, *Ann. Oncol.*, 1998, **9**, 39.
65 H. Maeda, J. Wu, T. Sawa, Y. Matsumura and K. Hori, *J. Controlled Release*, 2000, **65**, 271–284.
66 J. Li, J. H. Han, T. S. Xu, C. R. Guo, X. Y. Bu, H. Zhang, L. P. Wang, H. C. Sun and B. Yang, *Langmuir*, 2013, **29**, 7102–7110.